Scattering of Inertial Waves by Rough Bathymetry

DAVID RUBENSTEIN

Science Applications International Corporation, McLean, Virginia

(Manuscript received and in final form 8 June 1987)

ABSTRACT

Interactions between near-inertial waves and rough bathymetry are studied theoretically and numerically. Rough bathymetric features cause scattering, even when their length scales are much smaller than the wavelengths of the incident waves. The scattering efficiency depends on the relative slopes of the incident wave propagation and bottom features. Scattered wavelengths are comparable to wavelengths of the bathymetry. In a steady-state situation over an isolated bump, most of the kinetic energy is associated with upward propagating waves, in agreement with observations. A spectral model shows that first-mode incident waves with wavelengths > 150 km, and second-mode waves with wavelengths > 50 km are completely scattered into smaller wavelengths, primarily into wavelengths smaller than the bathymetry spectrum roll-off, 40 km. This model is applied to a spectrum of incident internal waves. The principal interactions involve the scattering of low-frequency, low-wavenumber incident waves into higher wavenumbers. Because of its higher wavenumbers, the scattered wave field has elevated shear levels and a Richardson number that is reduced by a factor of about 3.6 with respect to the incident wave field. A time-dependent numerical model simulates the evolution of wind-induced waves over rough bathymetry. All of the first vertical mode, containing about 35% of the initial energy, is scattered into higher modes after 40 inertial periods.

1. Introduction

Bathymetric profiles in the deep ocean show bumpy features over a wide range of length scales. It is possible that internal waves may suffer significant scattering through interactions with these features. The nature of these interactions depends on the relative scales of the internal waves and the bathymetric features.

When the scale of a bathymetric feature is much greater than that of an incoming internal wave, then the bottom acts as a uniformly sloping surface. Phillips (1963) and Eriksen (1982) developed theories of reflections by a uniform slope of infinite extent. We call this type of reflection "specular," because a monochromatic plane wave is reflected into a single direction with a single wavenumber—generally different from the incident wavenumber. Energy density, wavenumber, and azimuth angle are changed when an internal wave reflects off a sloping bottom. Eriksen (1985) showed that an isotropic model spectrum of internal waves is significantly altered by bottom reflection. Also, reflection drives shears to high values, and Richardson numbers to very low values. Therefore, reflection may be a potent mechanism for mixing near the bottom.

When the scale of a bathymetric feature is comparable to, or smaller than, an incoming wave, then the nature of the reflection is qualitatively different. Baines (1971a,b) found that in addition to a specularly reflected wave, forward and backward scattered waves are produced. The scattered wave components have wavenumbers that are different from that of the incident wave. The scattered wavenumbers are algebraic combinations of the incident wave and bathymetric wavenumbers. In the absence of mean flow, the frequencies and characteristic slopes of the incident, specularly reflected, and scattered waves are all equal in magnitude.

Mied and Dugan (1976) applied a high-order expansion solution to the scattering problem. Their results compared very well with Baines' solution, which involved only a first-order perturbation expansion. While Mied and Dugan's theory and method of solution are applicable to internal waves over a broad range of frequencies, they computed results only for high-frequency waves. This paper, on the other hand, is primarily concerned with the interactions of low-frequency, near-inertial waves with the ocean bottom. We will see that near-inertial waves interact much more strongly than do high-frequency waves, because the characteristic slopes of near-inertial waves are more nearly comparable to bathymetric slopes than are those of high-frequency waves. The objective of this paper is to quantify the strength of this interaction, and the time scale over which it operates on surface-forced waves.

Section 2 reviews results from Baines (1971a) for a single, isolated bump on the ocean floor. Because Baines chose not to present plots of his results, it is useful to look at a graphic of the energy modulation

Corresponding author address: Dr. David Rubenstein, Science Applications International Corp., P.O. Box 1303, McLean, VA 22102.

generated by a wave–bottom interaction. Section 3 begins with Baines' solution for a sinusoidal bottom and then extends the solution to a more general bathymetry profile using a Fourier series superposition approach. Section 4 applies the model developed in section 3 to an incident spectrum of internal waves. Section 5 examines the time-dependent evolution of a wind-induced inertial wave field, as it interacts with a sinusoidal bottom and more realistic bathymetry. Results are summarized and discussed in section 6.

2. Single, isolated bump

When an internal wave reflects off an isolated bump, it is scattered into wavelengths comparable to the scale of the bump. Baines (1971a) derived an expression for an incident plane wave, scattered by a bump with a particular profile. The spatial structure and the strength of modulation of the scattered wave are not readily apparent from Baines' expression. Therefore, it is of interest to evaluate the expression for a set of realistic, representative cases.

Following Baines (1971a), we consider an inviscid ocean, described by the equations of motion

$$\frac{\partial \mathbf{u}}{\partial t} + \mathbf{f} \times \mathbf{u} = -\frac{1}{\rho_0(z)} \nabla p - \frac{\rho g \mathbf{z}}{\rho_0(z)},$$

$$\nabla \cdot \mathbf{u} = 0,$$

$$\frac{\partial \rho}{\partial t} + w \frac{d\rho_0}{dz} = 0, \tag{2.1}$$

where x, y and z are Cartesian coordinates, with z directed upward, with corresponding velocity components u, v, and w; $\mathbf{z}$ is the unit vector in the direction of z, t is time, $\rho_0(z)$ is equilibrium density, p is perturbation pressure, ρ is perturbation density, g is the acceleration of gravity, and $\mathbf{f} = f\mathbf{z}$, where f is the Coriolis parameter. We assume that the wave motion and the bottom topography are independent of the y coordinate. Then the motion can be described in terms of a streamfunction $\psi(x, z, t)$, by the equations

$$u = -\frac{\partial \psi}{\partial z}, \quad w = \frac{\partial \psi}{\partial x}. \tag{2.2}$$

If we define a constant buoyancy frequency N by

$$N^2 = -\frac{g}{\rho_0}\frac{d\rho_0}{dz}, \tag{2.3}$$

then (2.1), (2.2) yield

$$\nabla^2 \psi_{tt} + N^2 \psi_{xx} + f^2 \psi_{zz} = 0. \tag{2.4}$$

We assume periodic time dependence of the form

$$\psi = \hat{\psi}(x, z) e^{-i\omega t}, \tag{2.5}$$

to obtain

$$\hat{\psi}_{xx} - s^2 \hat{\psi}_{zz} = 0, \quad s^2 = \frac{\omega^2 - f^2}{N^2 - \omega^2}, \tag{2.6}$$

where s is the characteristic slope. The general solution is of the form

$$\hat{\psi} = \hat{\psi}_1(\xi) + \hat{\psi}_2(\eta), \tag{2.7}$$

where $\hat{\psi}_1$ and $\hat{\psi}_2$ are complex-valued functions of the characteristic variables

$$\xi = z + sx, \quad \eta = z - sx. \tag{2.8}$$

The fluid is effectively infinite in depth with bathymetry

$$z = D(x), \tag{2.9}$$

where $D(x)$ is a smooth (differentiable) function, subject to the condition

$$|D'(x)| < s. \tag{2.10}$$

The magnitude of the bottom slope is everywhere smaller than the slope of the wave characteristics. The wave is not shadowed by the bathymetry.

This condition implies that there exists a one-to-one correspondence between the ξ and η characteristics, so that (2.9) can be written as either

$$\xi = -K(\eta), \quad \text{or} \quad \eta = -H(\xi), \tag{2.11}$$

where K and H are monotonically increasing functions. Baines imposes the asymptotic condition

$$D'(x) \to \alpha_\pm \quad \text{as} \quad x \to \pm\infty, \tag{2.12}$$

where $\alpha_\pm$ are constants, but we shall impose a more restrictive condition, that $\alpha_\pm = 0$.

The boundary condition at the bottom surface is $\psi = 0$. Baines showed that a solution of the form $\psi = \psi_i + \psi_t$ consisting of an incident plus a transmitted wave is not sufficient to satisfy radiation boundary conditions at infinity. Instead, a solution is assumed to have the form

$$\psi_i = \epsilon \exp[i(k\xi - \omega t)],$$

$$\psi_t = -\epsilon F_1(\eta) e^{-i\omega t},$$

$$\psi_r = \epsilon F_2(\xi) e^{-i\omega t}, \tag{2.13}$$

where $\psi = \psi_i + \psi_t + \psi_r$ is the sum of the incident, transmitted, and reflected waves, ϵ is an amplitude, and k is a total wavenumber. For a complete derivation of the results, the reader is referred to Baines (1971a). Here, we only present the result,

$$F_1(\eta) = \exp[-ikK(\eta)] + \mathcal{F}_2(\eta),$$

$$F_2(\xi) = \mathcal{F}_2[-H(\xi)] = \mathcal{F}_2(\eta). \tag{2.14}$$

Thus, the problem becomes one of determining the function $\mathcal{F}_2(\eta)$.

We consider a particular bump profile given by

$$K(\eta) = \eta + \frac{2da^2}{\eta^2 + a^2}, \tag{2.15}$$

where d is an amplitude and a is a length scale. We will only be considering bump profiles (not valleys). Therefore, the plus sign in (2.15) requires that $d < 0$. The slope condition (2.10) leads to the restriction

$$|d/a| < \frac{4}{3\sqrt{3}}. \tag{2.16}$$

Then an approximate solution for $\mathcal{F}_2(\eta)$ is given by

$$\mathcal{F}_2(\eta) = \frac{c_1(\eta/a - i) + c_2(\eta/a + i)}{(\eta/a)^2 + 1} + c_3\left[\frac{\eta/a - i}{(\eta/a)^2 + 1}\right]^2, \tag{2.17}$$

where

$$c_1 = -kde^{-ka}\left[1 - ikd(1 + ka) - \left(\frac{d}{a}\right)^2 \frac{1 - ikd(3/2 + ka)}{16 + (d/a)^2}\right],$$

$$c_2 = \frac{ikde^{-ka}}{4[1 + (d/4a)^2]}\left(\frac{d}{a}\right)[1 - ikd(3/2 + ka)],$$

$$c_3 = -(kd)^2 e^{-ka}. \tag{2.18}$$

This solution is accurate to second order in d/a and kd.

Figure 1 shows the normalized fields of kinetic energy density E/E_0 and phase $\Phi - \Phi_0$, where

$$E = \tfrac{1}{2}\rho uu^*,$$

$$\Phi = \arctan[\mathrm{Im}(u)/\mathrm{Re}(u)], \tag{2.19}$$

u is defined by (2.2), the asterisk denotes a complex conjugate, ρ is mass density, and E_0 and Φ_0 are the energy density and phase in the absence of a bump (flat topography). The normalization by E_0 and Φ_0 removes the modulation due to phase differentials across the width and height of the plots. The bump profile parameters in (2.15) are $d = -4$ m, $a = 10$ m. The wavenumber is $k = \pi/200$ m^{-1}, and the characteristic slope is $s = 1/100$. Therefore, the approximate vertical and horizontal wavelengths are $\lambda_z = 400$ m and $\lambda_x = 40$ km, respectively.

Because of the way that E and Φ are presented in Fig. 1, there are only two independent parameters, kd and d/a. For the case shown, $|kd| = \pi/50$ and $|d/a| = 0.4$. The coordinate axes are made nondimensional by λ_x and λ_z. Characteristic rays that intersect the origin also intersect the upper left and upper right corners of the plot frames. The full-width at half-height of the bump is equal to $2a/s = \lambda_x/20$, and the bump amplitude is $|d| = \lambda_z/100$. The amplitude-to-width ratio of the bump is $s|d|/2a = 2 \times 10^{-3}$.

Intuition from electromagnetic and acoustic waves tells us that when a scattering object is very much smaller than a wavelength, there should be no appreciable scattering effect. However, Fig. 1 shows that for internal gravity waves, this is not the case. The kinetic energy and phase fields show strong modulations along the two characteristic rays emanating from the center

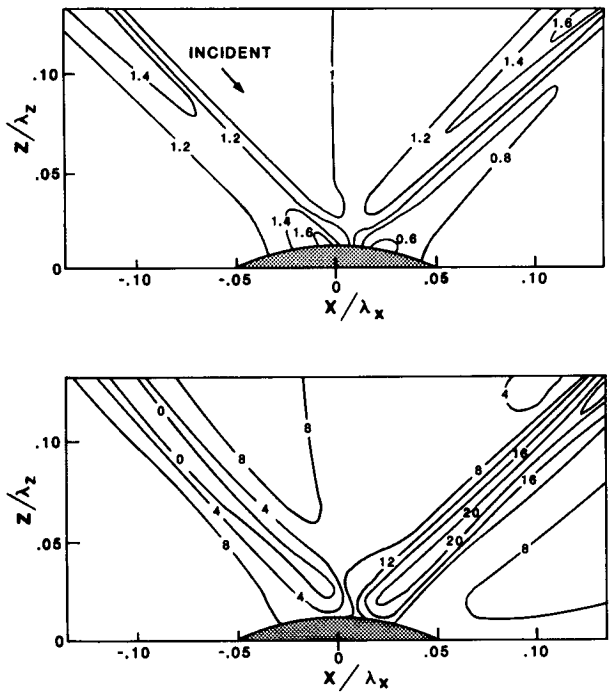

FIG. 1. Contours of normalized kinetic energy E/E_0 (upper) and relative phase $\Phi - \Phi_0$ (lower). Contour increment for phase is 4°. The horizontal and vertical coordinate axes are scaled by the horizontal and vertical wavelengths. Parameter values are $d/\alpha = -0.4$ and $kd = \pi/50$. The bump profile is shown at the bottom. Plane internal waves are incident on the bump, coming from the upper left corner. Back-scattered and forward-scattered waves propagate toward the upper left and right corners, respectively.

of the bump. Additional computations (not presented here) using much lower wavenumbers give results that are qualitatively very similar to Fig. 1. Therefore, phase interference effects due to the finite—but very small—size of the bump do not contribute appreciably to the scattering pattern. Instead, scattering is primarily a result of the fact that the slope of the bump is significant in comparison with the wave characteristic slope, s.

One way to see this is to analyze the $\exp[-ikK(\eta)]$ component term of ψ in (2.14). With $K(\eta)$ given by (2.15), this term becomes

$$\exp(-ik\eta)\exp\left[-ik\left(\frac{2da^2}{\eta^2 + a^2}\right)\right].$$

The term in parentheses in the second exponential has a maximum value $2d$ for $\eta = 0$. Therefore, the maximum phase modulation due to the second exponential is $\exp(-2ikd)$, which is small because $|kd| \ll 1$. However, the derivative is

$$\frac{d}{d\eta}\exp[-ikK(\eta)] = -ik\left(1 - \frac{4da^2\eta}{(\eta^2 + a^2)^2}\right)\exp[-ikK(\eta)]. \tag{2.20}$$

The maximum magnitude of $4da^2\eta(\eta^2 + a^2)^{-2}$ is equal to $(3\sqrt{3}/4)|d/a|$, for $\eta = \pm a/\sqrt{3}$. When d/a is of order one, the term in parentheses in (2.20) is strongly modulated in the vicinity of $-a \leq \eta \leq a$. From the above discussion, we conclude that the streamfunction ψ is not significantly altered by the presence of the bump. However, the velocity component $u = -\partial\psi/\partial z = -\partial\psi/\partial\eta$ is strongly modulated, because the slope of particle motions is comparable to—but smaller than—the slope of the bottom topography.

The phase contours in Fig. 1 can be used to infer the direction of the propagating energy. Regions where the phase increases (decreases) with depth indicate that the inertial velocity vector rotates anticlockwise (clockwise) with depth, hence upgoing (downgoing) energy dominates. Careful comparison of the upper and lower frames in Fig. 1 shows that regions where $E/E_0 > 1$ ($E/E_0 < 1$) coincide with net upgoing (downgoing) energy, and where $E/E_0 = 1$ there is equality. Therefore, in the vicinity of a bump, most of the kinetic energy is associated with upward propagating waves. These results, discussed in greater detail in section 6, are in agreement with observations of near-inertial waves over a seamount by Kunze and Sanford (1986).

3. Statistical model of bottom scattering: Monochromatic incident wave

In this section we consider a statistical representation of bottom topography. We first deal with the scattering of a monochromatic internal wave by a small amplitude sinusoidal bottom. Then we assume that the ocean bottom can be represented as a random-phase Fourier superposition, with amplitudes determined by an empirical spectrum. We derive a spectrum of scattered internal waves. By integrating this spectrum we arrive at the total fraction of energy flux that is scattered from the incident wavelength into all other wavelengths.

a. Single wavenumber incident on sinusoidal bathymetry

We consider a sinusoidal bottom topography that is invariant in the y direction,

$$D(x) = d\cos lx, \tag{3.1}$$

where d is amplitude and l is wavenumber. An incident monochromatic wave propagating in the x-direction is defined by the streamfunction

$$\psi_i = \epsilon \exp[i(k\xi - \omega t)], \tag{3.2}$$

where k is total wavenumber and ξ is defined by (2.8). The amplitude d is subject to the restrictions

$$kd \ll 1, \quad ld \ll 1. \tag{3.3}$$

To first-order accuracy in kd and ld, the reflected and transmitted streamfunctions (2.13) may be written in terms of $F_1(\eta)$ and $F_2(\xi)$ as

$$F_1(\eta) = (1 - k^2d^2)e^{-ik\eta} + ikd\{\exp[-i\eta(l/s + k)] + \exp[-i\eta(k - l/s)]\},$$
$$F_2(\xi) = 0, \tag{3.4a}$$

for $l < sk$, and

$$F_1(\eta) = (1 - kd^2l/s)e^{-ik\eta} + ikd\exp[-i\eta(l/s + k)],$$
$$F_2(\xi) = -ikd\exp[-i\xi(l/s - k)], \tag{3.4b}$$

for $l > sk$. This result is essentially the same as that derived by Baines (1971a). This solution contains a specular reflection component which has a wavenumber k unchanged from that of the incident wave. A sum wavenumber $k + l/s$ is forward-scattered and a difference wavenumber $|k - l/s|$ is forward-scattered for $l < sk$, and back-scattered for $l > sk$.

Equation (3.4) is accurate to first order in kd and ld. A perturbation expansion to higher order yields an infinite set of discrete, scattered wavenumbers,

$$k' = |k \pm nl/s|; \quad n = 1, 2, 3, \cdots, \tag{3.5}$$

and the amplitudes of these components are proportional to $(kd)^n$. In this section, we will consider only the first-order $n = 1$ contributions.

The vertical energy flux of the incident wave (3.2) is given by

$$\mathbf{F}_i = \frac{1}{2}\rho\epsilon^2 k\frac{[(\omega^2 - f^2)(N^2 - f^2)]^{1/2}}{\omega}, \tag{3.6}$$

and the vertical energy fluxes of the sum (+) and difference (−) scattered components are given by

$$\mathbf{F}_\pm = \frac{1}{2}\rho\epsilon^2|k \pm l/s|sk^2d^2\frac{[(\omega^2 - f^2)(N^2 - f^2)]^{1/2}}{\omega}. \tag{3.7}$$

The ratio of (3.7) to (3.6) is simply

$$\mathbf{F}_\pm/\mathbf{F}_i = |k \pm l/s|kd^2. \tag{3.8}$$

b. Single wavenumber incident on general bathymetry

Now let us consider a general bathymetric profile $D(x)$ of finite length X. The Fourier transform of $D(x)$ is

$$\hat{D}(l) = \int_0^X D(x)e^{-2\pi ilx}dx, \tag{3.9}$$

and the associated power spectrum $S(l)$ is given by

$$S(l) = 2\lim_{X\to\infty}\frac{1}{X}\langle|\hat{D}(l)|^2\rangle, \tag{3.10}$$

where angled brackets denote expected value. Because the spectrum of a sinusoid (3.1) is

$$S(l_0) = \frac{\langle d^2\rangle}{2}\delta(l - l_0), \tag{3.11}$$

we make the identification

$$\langle \mathbf{F}_{\pm}/\mathbf{F}_i \rangle = |k \pm l/s|k\langle d^2 \rangle = 2|k \pm l/s|kS(l)dl. \quad (3.12)$$

Then the probability per unit wavenumber that energy flux will be scattered from wavenumber k to some other wavenumber k', is given by

$$\hat{p}(k, k') = \sum_{+,-} 2 \int_0^\infty |k \pm l/s|kS(l)\delta(k' - |k \pm l/s|)dl$$

$$= 2k'k\{S[s|k' - k|] + S[s(k' + k)]\}. \quad (3.13)$$

There is no reason in principle why

$$\hat{P} = \int_0^\infty \hat{p}(k, k')dk' \quad (3.14)$$

should always be less than one. Therefore, we define a total probability density function $p(k, k')$ in such a way that flux conservation is ensured,

$$p(k, k') = A\hat{p}(k, k') + B\delta(k' - k), \quad (3.15)$$

where

$$A = \begin{cases} 1 \\ \hat{P}^{-1} \end{cases}, \quad B = \begin{cases} 1 - \hat{P} \\ 0 \end{cases}, \quad \text{if} \quad \hat{P} \begin{cases} \leqslant 1 \\ \geqslant 1 \end{cases}. \quad (3.16)$$

The second term in (3.15) denotes the contribution due to specular reflection (wavenumber is unchanged). According to (3.16), the specular reflection contribution is simply the remainder after all the scattered flux has been removed from the original monochromatic incident wave.

We take for $S(l)$ an empirical model spectrum introduced by Bell (1975a), modified in a minor way with an abrupt high wavenumber cutoff,

$$S(l) = \begin{cases} S_0(l^2 + l_0^2)^{-1}, & l \leqslant l_c \\ 0, & l > l_c, \end{cases} \quad (3.17)$$

where $S_0 = 250$ m^2 cpkm, $l_0 = 0.025$ cpkm, and $l_c = 2.5$ cpkm.

Following Munk (1981), we use an approximate expression for vertical wavenumber,

$$k_z = \frac{j}{2b}\left(\frac{N^2 - \omega^2}{N_0^2 - \omega^2}\right)^{1/2} \text{ (cpkm)}, \quad (3.18)$$

where j is a mode index, $b = 1.3$ km is the e-folding scale of $N(z)$, and $N_0 = 3$ cph is the surface extrapolated buoyancy frequency. We choose $N = 0.5$ cph as the local buoyancy frequency, near the ocean bottom.

Table 1 shows the fraction of vertical energy flux scattered out of the incident wavenumber, defined by $1 - B$, as a function of horizontal wavelength and vertical mode index. This quantity is equal to one for all but the smallest horizontal wavelengths and vertical modes. This result is important. All of the energy flux incident with horizontal wavelengths $\geqslant 150$ km is immediately scattered into other wavelengths.

This analysis is based on the solution (3.4), which is valid subject to the condition of no wave shadowing (2.10). For the sinusoid bottom profile (3.1), this condition becomes

$$s > ld. \quad (3.19)$$

With the ensemble of Fourier transforms (3.9), (3.10), this condition cannot be met with absolute certainty for any specific incident wave. Instead, we can only conform with (3.18) in a probabilistic sense. We might stipulate, for example, that

$$s > 2\sigma_s, \quad (3.20)$$

where σ_s is the rms bottom slope. For the model spectrum given by (3.17), $\sigma_s = 0.025$. Therefore, the elements in Table 1 that disobey (3.20) are enclosed in parentheses. One would intuitively conjecture, though, that shadowing can only act to increase the modulating effect on the reflecting waves.

TABLE 1. Fraction of vertical energy flux scattered out of incident wavenumber.

Vertical mode index	Incident horizontal wavelength (km)			
	25	50	100	200
1	0.05	0.13	0.49	1
2	0.31	1	1	(1)
3	1	1	1	(1)

Figures 2 and 3 show the distributions of scattered energy flux for modes 1 and 2, respectively. The upper frames of the figures display plots of $p(k, k')$ given by (3.15). Spikes associated with specular reflection are not shown. The peaks in these functions lie within the wavelength range from 10 to 40 km. The upper limit of this range corresponds to the spectral roll-off wavenumber $l_0 = 0.025$ cpkm, in (3.17).

The lower frames of Figs. 2 and 3 display the cumulative probability distributions $\int_0^{k'} p(k, \beta)d\beta$. Discontinuous jumps in these curves are associated with the fraction of specular reflection, i.e., the parameter B in (3.15). Because the 200 km, first mode wave is not subject to specular reflection, it shows no discontinuous jump in Fig. 2. The probability distributions for longer wavelength and higher mode waves are virtually identical. For these distributions, about 7% of the energy flux is scattered into the wavelength range 40 to 100 km, and about 31% is scattered into each of the wavelength ranges 10–40 km, 2–10 km, and 0.4–2 km.

4. Statistical model of bottom scattering: Spectrum of incident internal waves

So far, we have considered the scattering of a single internal wave incident on a rough bottom. Qualitatively, we found that there is a transfer of energy flux in different, predominantly higher wavenumbers. The

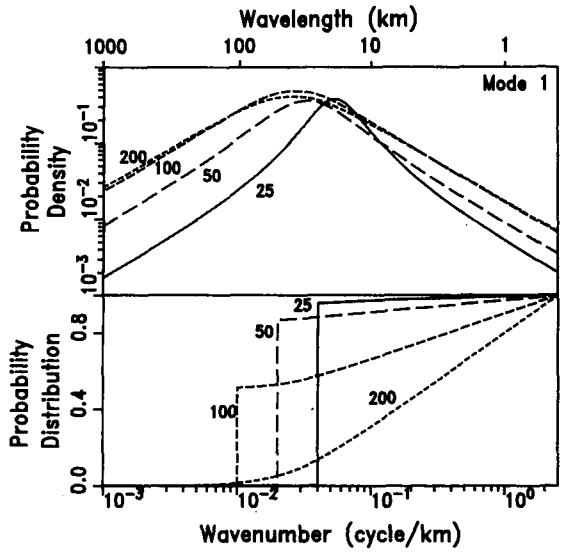

FIG. 2. Probability density and probability distribution of scattered energy flux, of first vertical mode, for 25, 50, 100 and 200 km incident waves. Spikes associated with specular reflection are not shown in the probability density, but do show up as discontinuous steps in the probability distribution. These steps represent fraction of energy that is specularly reflected.

resulting effect on a spectrum of incident waves is not immediately apparent. In this section we will see how a model spectrum of energy flux density of internal waves is altered by the scattering mechanism.

The method of approach is similar to that of Eriksen (1985). We assume that the Garrett–Munk (GM) model of the internal wave spectrum is applicable in the deep ocean, at some distance from the bottom. The vertical energy flux can be equally partitioned into upgoing and downgoing waves. We take the downgoing waves to be incident on a rough bottom with a model spectrum given by (3.17). The spectrum of scattered (upgoing) energy flux will be different from that of the incident (downgoing) flux. We assume that unspecified adjustment processes (such as nonlinear mixing) act to redistribute the upgoing flux spectrum back into the canonical GM model form.

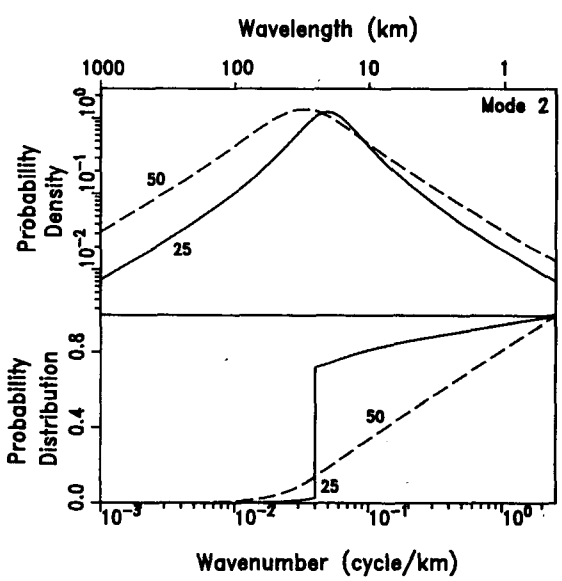

FIG. 3. As in Fig. 2 except for second vertical mode, for 25 and 50 km incident waves.

Following Munk (1981), we model the spectrum of internal waves as summarized by

$$E(\omega, j) = B(\omega)H(j)E, \tag{4.1}$$

$$B(\omega) = \frac{2f}{\pi\omega}(\omega^2 - f^2)^{-1/2}, \tag{4.2}$$

$$H(j) = (j^2 + j_*^2)^{-1} / \sum_{j=1}^{\infty} (j^2 + j_*^2)^{-1}, \tag{4.3}$$

$$\sum_{j=1}^{\infty} H(j) = 1, \tag{4.4}$$

where

$$k_z = \frac{j\pi}{b}\left(\frac{N^2 - \omega^2}{N_0^2 - \omega^2}\right)^{1/2} \tag{4.5}$$

is the local vertical wavenumber corresponding to mode j, $j_* = 3$ is a cutoff mode number, $B(\omega)$ and $H(j)$ are separable frequency and wavenumber shapes, and $E = 6.3 \times 10^{-5}$ is a constant spectral level. The energy spectral density per unit mass, frequency, and wavenumber is given by

$$S_e(\omega, j) = b^2 N_0 N E(\omega, j), \tag{4.6}$$

where $b = 1.3$ km is a stratification scale height, $N_0 = 3$ cph is the surface-extrapolated buoyancy frequency, and $N = 0.5$ cph is the local buoyancy frequency. The spectral density of the vertical component of flux incident on the bottom is given by

$$\mathbf{F}_i(\omega, j) = -(\rho_0/2)E(\omega, j)c_z(\omega, k_z), \tag{4.7}$$

where ρ_0 is density and c_z is the vertical component of group velocity. Ultimately what we desire is an expression for the scattered vertical flux $\mathbf{F}_s$,

$$\mathbf{F}_s(\omega, k') = \int_0^{\infty} \mathbf{F}_i(\omega, k)p(k, k')dk, \tag{4.8}$$

in terms of the incident flux $\mathbf{F}_i$ and the probability density p defined in (3.13)–(3.15). But because the spectral model is in terms of discrete modes, we must transform (3.13)–(3.15) from a continuous wavenumber form into modal form:

$$\begin{aligned}\hat{p}(j, j') &= 2\alpha jj'\{S[s|j' - j|] + S[s(j' + j)]\} \\ &\equiv \hat{p}_-(j, j') + \hat{p}_+(j, j'),\end{aligned} \tag{4.9}$$

$$\hat{p}_{\pm}(j, j') = \begin{cases} \dfrac{2S_0}{s^2} \dfrac{jj'}{(j \pm j')^2 + (l_0/s\alpha)^2}, & |j \pm j'| \leq L_c \\ 0, & |j \pm j'| > L_c, \end{cases} \tag{4.10}$$

$$\hat{P} = \alpha \sum_{j'=0}^{\infty} \hat{p}(j, j'), \tag{4.11}$$

$$p(j, j') = A\hat{p}(j, j') + B\delta(j' - j), \tag{4.12}$$

$$L_c = l_c/s\alpha, \tag{4.13}$$

where A and B are defined by (3.16), j and j' are the mode indices for incident and scattered wave components, respectively, and we have made use of the definition of the modal (total) wavenumber

$$k_j \equiv \alpha j = \frac{\pi}{b}\left(\frac{N^2 - f^2}{N_0^2 - \omega^2}\right)^{1/2} j. \tag{4.14}$$

Adjusting summation limits, the expression for $\hat{P}$ given by (4.11) becomes

$$\hat{P} = \alpha \sum_{j'=j_1}^{j_2} \hat{p}_{-}(j, j') + \alpha \sum_{j'=j_3}^{j_4} \hat{p}_{+}(j, j'), \tag{4.15}$$

where

$$j_1 = \max\{1, j - L_c\}, \quad j_2 = \min\{j + L_c, J_{\max}\},$$
$$j_3 = 1, \qquad\qquad j_4 = \min\{L_c - j, J_{\max}\}, \tag{4.16}$$

where $J_{\max}$ is the maximum mode of the spectral model. Then our expression for the spectral density of scattered vertical energy flux in (4.8) becomes

$$\mathbf{F}_s(\omega, j') = \alpha A \sum_{j=j_1'}^{j_2'} \mathbf{F}_i(\omega, j)\hat{p}_{-}(j, j') + \alpha A \sum_{j=j_3'}^{j_4'} \mathbf{F}_i(\omega, j)\hat{p}_{+}(j, j') + B\mathbf{F}_i(\omega, j'), \tag{4.17}$$

where the summation limits are given by (4.16), with the primed and unprimed values of j interchanged.

The results shown in Fig. 4 were computed for an array of $J_{\max} = 32$ discrete modes and 32 frequencies scaled logarithmically between the local inertial frequency $f = 10^{-4}$ s^{-1} and the local buoyancy frequency $N = 0.5$ cph. As the bottom-scattering mechanism does not alter the frequency from that of the incident wave, the chosen number of frequencies is not materially significant to the present calculations: a large number simply serves to make the plotted results appear continuous. In contrast, the chosen number of discrete modes affects the spectrum of incident vertical flux through the summation limit in the expression for the shape function $H(j)$ given in (4.3).

Figure 4a shows the GM model spectrum of incident flux $\mathbf{F}_i(\omega, j)$. The spectrum of scattered flux $\mathbf{F}_s(\omega, j)$ is shown in Fig. 4b. It is difficult to compare Figs. 4a and 4b directly, so the reader's attention is directed to Fig. 4d, which shows the ratio of scattered-to-incident flux spectra. In the low-frequency range, near the inertial frequency, energy is strongly scattered from low wavenumbers (low vertical mode) into higher wavenumbers. This result is indicated by the sharp dip in the right corner of the plot (low frequencies and low modes), and by the general rise in the upper corner (low frequencies and high modes). In the high-frequency range, near the buoyancy frequency, the ratio is nearly unity. Weak scattering at high frequencies causes very little redistribution of energy flux.

Figure 4c shows the fraction $1 - B$ of flux that is scattered into some other wavenumber. The value of this fraction is unity throughout most of the area in frequency–wavenumber space, except for a small triangular area at low wavenumbers and high frequencies. This result indicates that 100% of the flux incident on a rough bottom gets scattered to some other wavenumbers, except for incident wave packets with a combination of high frequency and low wavenumber, which are not strongly affected by rough bottom scattering. The ratio of scattered-to-incident flux in Fig. 4d is nearly level in this region.

Figure 5 shows the energy spectra projected into wavenumber and frequency space, partitioned into incident (half the GM spectrum) and scattered components. From the wavenumber spectrum, it is clear that energy is scattered from low wavenumbers into high wavenumbers. The crossover mode index is $j = 10$ ($\sim$1500 m local vertical wavelength). Defining the effective modal bandwidth j_e by

$$j_e = [\sum S(j)]^2 / \sum S(j)^2, \tag{4.18}$$

we then get $j_e = 9$, 28, and 14 for the incident, scattered, and incident plus scattered energy spectra, respectively. Using Fu's (1981) definition of coherence scale,

$$\Delta z_{1/2} = \frac{2bN_0}{j_e \pi N(z)}, \tag{4.19}$$

we get $\Delta z_{1/2} = 555$, 180 and 360 m, respectively.

The frequency spectrum in Fig. 5 shows that the scattered component is slightly weaker than the incident component in the near-inertial range. The scattered and incident components are nearly equal in magnitude at higher frequencies.

Munk (1981) introduced a reciprocal Richardson number, which Pinkel (1985) generalized to an inverse Richardson function, defined by

$$\mathrm{Ri}^{-1}(\omega, k) = N^{-2} \int_{k_{\min}}^{k} \int_{\omega_{\min}}^{\omega} \Phi(\hat{\omega}, \hat{k}) d\hat{\omega} d\hat{k}, \tag{4.20}$$

where $\Phi(\hat{\omega}, \hat{k})$ is shear spectral density. We can write this expression in terms of the discrete mode GM model spectrum,

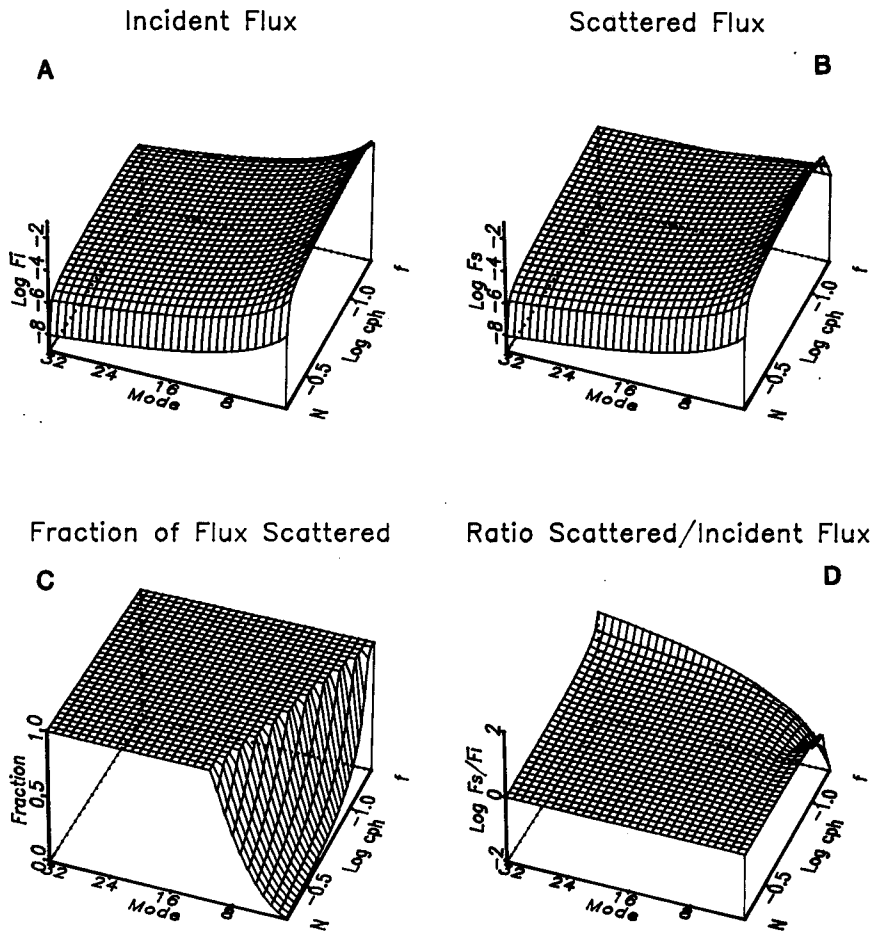

FIG. 4. (a) Spectrum of incident energy flux, shown as a function of vertical mode number ranging from 1 to 32, and of frequency, ranging from the local inertial frequency $f = 10^{-4}$ s^{-1} to the local buoyancy frequency N = ½ cph = 8.7×10^{-4} s^{-1}. (b) Spectrum of scattered flux as predicted by spectral model. (c) Fraction of flux which, when incident at a given frequency and wavenumber, is scattered into some other wavenumber. (d) Ratio of scattered-to-incident flux spectra.

$$\mathrm{Ri}^{-1}(\omega, j) = N^{-2} \int_f^{\omega} d\hat{\omega} \sum_{\hat{j}=1}^{j} \frac{\hat{\omega}^2 + f^2}{\hat{\omega}^2} S_e(\hat{\omega}, \hat{j}) k_z^2(\hat{\omega}, \hat{j}). \tag{4.21}$$

This function is a description of the cumulative shear spectrum, normalized by the stratification. It has the advantage of having an intuitive interpretation in terms of the tendency toward shear instability. This function was evaluated at three frequencies, $\omega = 1.08f$, $1.33f$, $8.72f \approx N$, as shown in Fig. 6. The maximum mode index, $J_{\max} = 100$, was chosen to be comparable with measurements described here. The solid and dashed curves correspond to the incident and scattered spectra, respectively. The value of $\mathrm{Ri}^{-1}(\omega, j)$ of the scattered wave field is smaller than that of the incident wave field for low modes, and is greater for high modes. The crossover for $\omega \approx N$ occurs at mode index $j \approx 15$ (~1000 m local vertical wavelength). This behavior simply reflects the ratio of scattered-to-incident flux spectra, shown in Fig. 4d. Most of the contribution to $\mathrm{Ri}^{-1}(N, j)$ comes from near-inertial frequencies, which are most strongly scattered. High frequency waves are only weakly scattered, and also do not contribute much to $\mathrm{Ri}^{-1}(N, j)$. The values of $\mathrm{Ri}^{-1}(N, J_{\max} = 100)$ are 0.03 and 0.11 for the incident and scattered wave fields, respectively.

The shape of the $\mathrm{Ri}^{-1}(\omega, j)$ function depends in a nontrivial way on the value chosen for $J_{\max}$. The reason for this is that the wavenumber shape function $H(j)$, defined by (4.3) and (4.4), depends on $J_{\max}$. However, Munk (1981) showed that the integrated value $\mathrm{Ri}^{-1}(N, J_{\max})$ is approximately proportional to $J_{\max}$, at least up to a spectral break observed in the upper ocean at 0.1 cpm (Gargett et al., 1981). For upper-ocean near-inertial waves, this wavenumber corresponds to $j = 260$. For this maximum mode index, we calculate that $\mathrm{Ri}^{-1}(N, J_{\max} = 260)$ is equal to 0.08 and 0.29 for the incident and scattered wave fields, respectively.

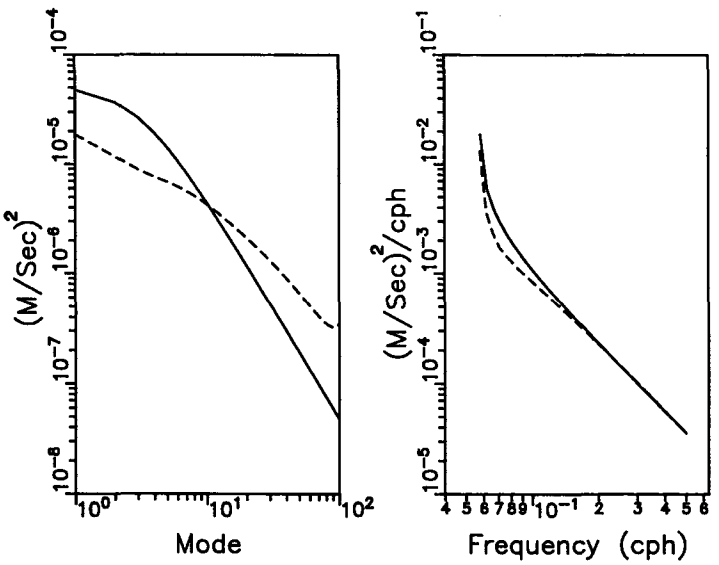

FIG. 5. Energy spectra projected into wavenumber (left) and frequency (right) space. Solid curves denote incident wave field, and dashed curves denote scattered wave field.

As a point of reference, we can compare these results with Pinkel's (1985) measurements of the inverse Richardson function, computed from Doppler sonar velocity profiles in the upper ocean. His upper wavenumber cutoff of 1/28 cpm corresponds to a maximum mode index $J_{max} \approx 100$. His offshore and alongshore components of reciprocal Richardson number exceed our incident $\mathrm{Ri}^{-1}(N, J_{max} = 100)$—which includes just the incident wave field—by factors of ≈ 10 and ≈ 14, respectively. We should account for the fact that (4.20) is proportional to N/N_0, and that the local buoyancy frequency is greater by a factor of ≈ 7 in the upper ocean. Therefore, the normalized shear level in the upper ocean was actually greater than the GM spectral level by a factor of 1.5–2, and smaller than the scattered wave level by a factor 2–2.5. Pinkel mentions that much of the high frequency shear might not be due to internal waves; however, the high frequency contribution to the reciprocal Richardson number is relatively small.

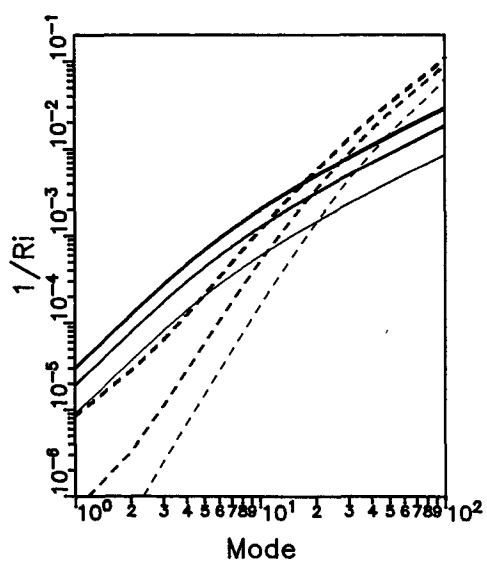

FIG. 6. Inverse Richardson function, for incident (solid) and scattered (dashed) wave fields. The function was evaluated at three frequencies, $\omega = 1.08f$, $1.33f$ and $8.72f \approx N$, corresponding to the thin, medium, and thick curves.

5. Response to surface forcing

a. Model formulation

In this section we study the problem of bottom interactions in the time domain. We formulate an initial value problem, in which a wind stress has initially deposited momentum into a surface mixed layer. The mixed layer is dynamically coupled with a stratified, inviscid interior. Near-inertial internal waves propagate into the interior, and scatter off the rough bottom.

The model formulation is similar to the internal wave model of Rubenstein and Roberts (1986) and is not repeated here. There are two significant differences between the application of the model reported here and in Rubenstein and Roberts. Instead of a uniform, level bottom, we implement variable bathymetry $D(x)$, and the top and bottom boundary conditions are

$$w = 0 \quad \text{at} \quad z = 0,$$
$$w = uD'(x) \quad \text{at} \quad z = -D(x), \tag{5.1}$$

where u and w are the velocity components in the x and z (positive upward) coordinate directions. A second

difference is that instead of radiation-absorbing lateral boundary conditions, we implement reflecting lateral boundaries. The interior velocities u and v and mixed layer velocities $\bar{u}$ and $\bar{v}$ are antisymmetric, and buoyancy b is symmetric with respect to the lateral boundaries at $x = \pm\pi k_x^{-1} = \pm 100$ km. Therefore, the solution is periodic in x, with wavelength $2\pi k_x^{-1} = 200$ km.

b. Model parameters

The initial condition is of the form

$$\bar{v} = \bar{v}_0 \sin k_x x, \tag{5.2}$$

where $\bar{v}$ is the mixed layer velocity in the y-coordinate direction, and $\bar{v}_0 = 1$ m s^{-1}. We will call k_x the "primary" wavenumber. The initial mixed layer depth is 200 m. Because of its convenient properties, we choose a mean buoyancy frequency profile similar to that of Gill (1984):

$$N(z) = \begin{cases} 0, & -h < z < 0 \\ \gamma(z_0 - z)^{-1}, & -D < z < -h, \end{cases} \tag{5.3}$$

where $\gamma = 2.8$ m s^{-1} and $z_0 = 150$ m.

c. Case 1: Sinusoidal bottom profile

Case 1 involves a sinusoidal profile given by

$$D(x) = D_0 + d \cos lx, \tag{5.4}$$

where $D_0 = 5$ km is mean depth, $d = 100$ m is amplitude, and l is wavenumber. To achieve simple periodicity, we require that the profile wavenumber l be an integer multiple of the initial condition wavenumber,

$$l = jk_x. \tag{5.5}$$

We will take the particular case of $j = 4$; $2\pi l^{-1} = 50$ km.

Figure 7 displays the solution fields $w(x, z)$ at time $t = 4$ inertial periods, with and without bathymetry. The solution for w emphasizes the horizontal variability of the internal wave motions. There is strong $\approx$50 km wavelength modulation of the w field, especially in the deeper half of the model basin.

In order to quantify the scattering effect, horizontal wavenumber spectra of the horizontal currents were computed. The periodic nature of the solution allows us to use standard fast Fourier transform procedures to compute spectral density functions. This approach is facilitated by the fact that the horizontal grid dimension (64 internal grid points) is a power of two.

The spectral density function of the initial velocity distribution (5.2) is given by

$$S(k_x) = \pi\bar{v}_0^2/k_x = 100 \text{ m}^2 \text{ s}^{-2} \text{ cpkm}^{-1}. \tag{5.6}$$

If there is no bathymetry (flat bottom) then as the system evolves in time, all of the energy remains at the k_x wavenumber. With the sinusoidal bathymetry (4.14), energy is scattered into the wavenumbers

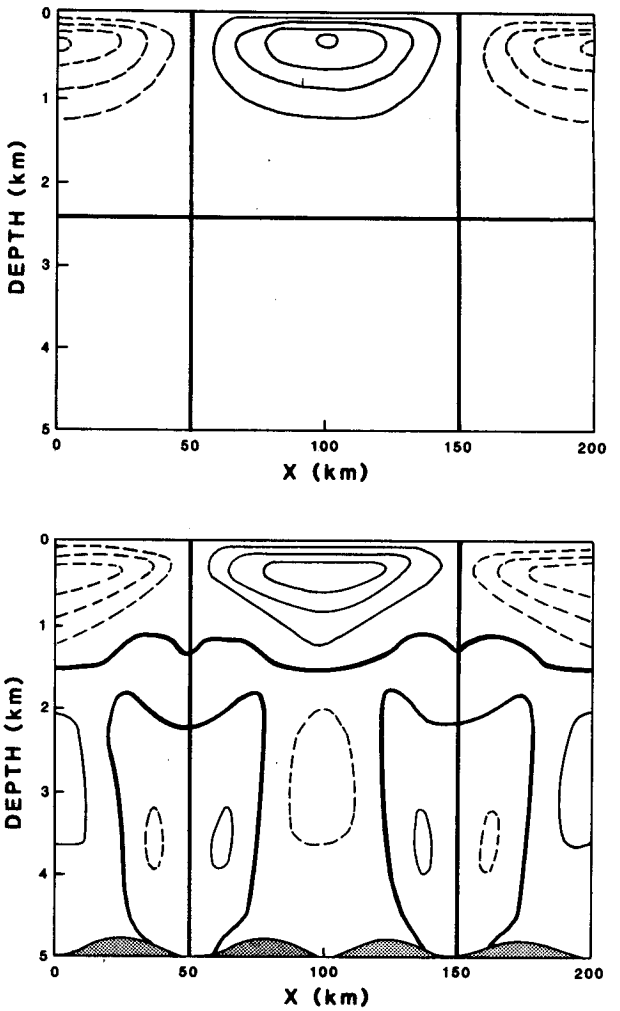

FIG. 7. Contours of vertical velocity w, after four inertial periods model simulation, for flat bathymetry (top) and sinusoidal bathymetry (bottom). Thick curves denote zero, solid/dashed curves denote positive/negative contours. The contour increment is 0.08 cm s^{-1}. The wavelength of the initial condition is 200 km.

$$k_x' = |k_x \pm nl|; \quad n = 1, 2, 3, \cdots. \tag{5.7}$$

Note the similarity to (3.5). Due to computational noise, energy is also scattered into other wavenumbers. These energy levels are orders of magnitude smaller than the levels at the scattered wavenumbers given by (5.7) and will not be considered further.

Figure 8 displays the evolution of spectral density profiles for the primary wavenumber $k_x' = k_x$, and for the first-order scattered wavenumbers $k_x' = k_x \pm l$. Profiles are shown at times $t = 4$, 8, 12, and $16t_i$, where $t_i = 2\pi/f$ is an inertial period (17.45 h). The scattered wavenumber profiles of energy density are generally about two orders of magnitude below that of the primary wavenumber. From the number of "dips" in the profiles, we note that higher order vertical modes are more visible in the scattered profiles than in the pri-

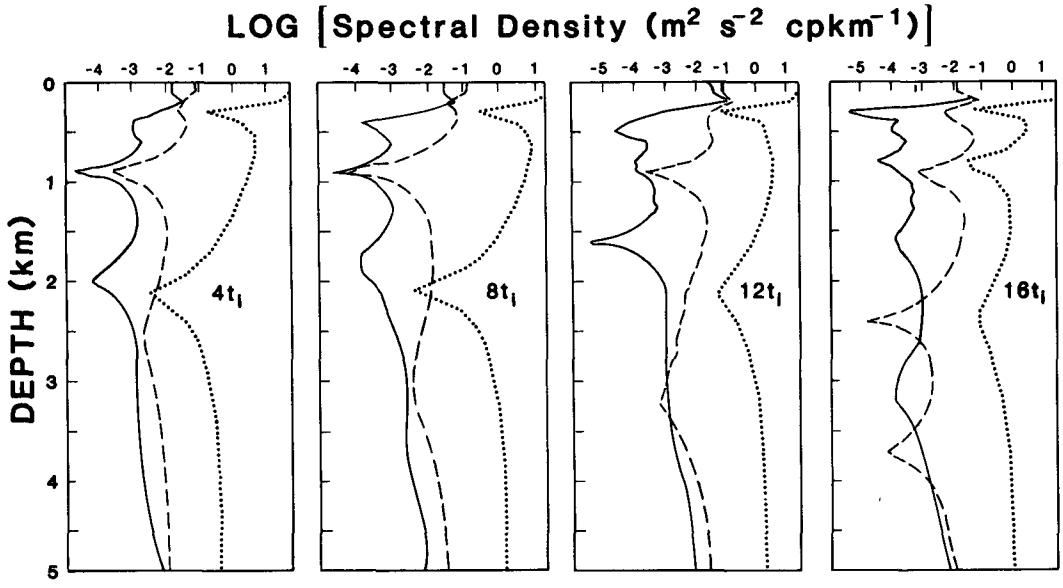

FIG. 8. Evolution of spectral density profiles at times 4, 8, 12 and 16 inertial periods. Dotted curves denote primary $k'_x = k_x$ wavenumber, dashed curves denote $k'_x = k_x - l$, solid curves denote $k'_x = k_x + l$.

mary profile. This is expected, because the bottom scatters energy into higher wavenumbers.

How does the bumpy bottom affect the energy density at the primary wavenumber? Figure 9 shows a comparison of time histories of the spectral energy density at three depths at wavenumber $k'_x = k_x$, for simulations with a flat, level bottom ($d = 0$), and the case 1 bumpy bottom. In order to suppress the rapid modulations due to inertial oscillations, a low-pass filter has been applied. The rapid oscillations that remain, with a period of about $4t_i$, result from the beating of the first vertical mode with purely inertial oscillations (Gill, 1984; Kundu and Thomson, 1985). The slower envelope oscillations result from the beating of low-order modes with inertial oscillations. For the first $8t_i$ or so, the comparison shows virtually identical results. As time elapses beyond $30t_i$, about ⅓ to ½ of the energy is depleted from the primary wavenumber, through bottom interactions. The first vertical mode separates from the initial profile sooner than do the higher modes. Therefore, the first mode—which initially contains about 35% of the energy—interacts with the rough bottom most rapidly. As a result the rapid oscillations decay and the slower oscillations associated with the higher modes dominate after about $40t_i$.

d. *Case 2: Realistic bottom profile*

For case 2 we use a realistic bottom profile, simulated using a truncated Fourier series

$$D(x) = D_0 + \sum_{j=1}^{N} d_j \cos(jk_x x + \varphi_j), \qquad (5.8)$$

where the amplitudes are given by

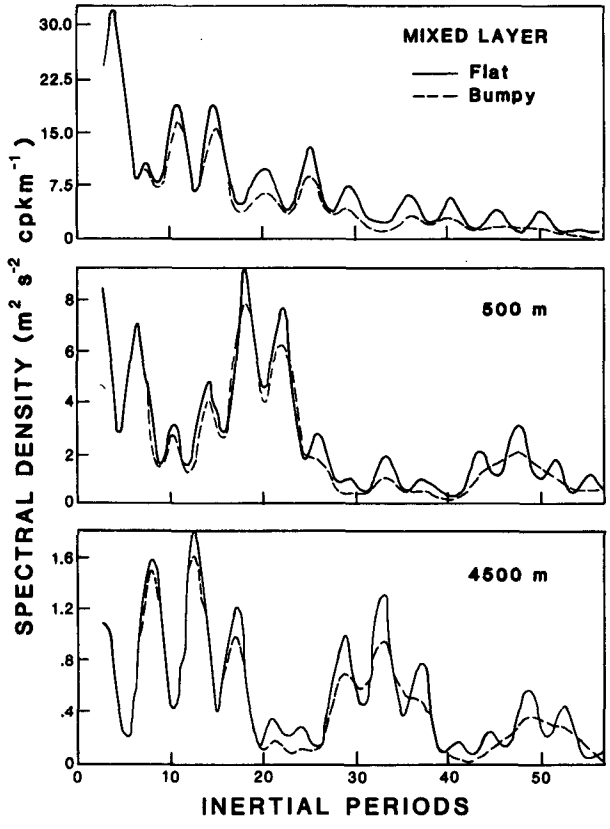

FIG. 9. Evolution of spectral density in the mixed layer, at 500 m and at 4500 m depth, for the flat bathymetry case (solid) and for the sinusoidal bathymetry case (dashed). A low-pass filter has been applied to remove inertial oscillations. The $4t_i$ oscillations which remain are due to beating between pure inertial oscillations and the first vertical mode. These oscillations dissipate with time, as the first mode is scattered into higher modes.

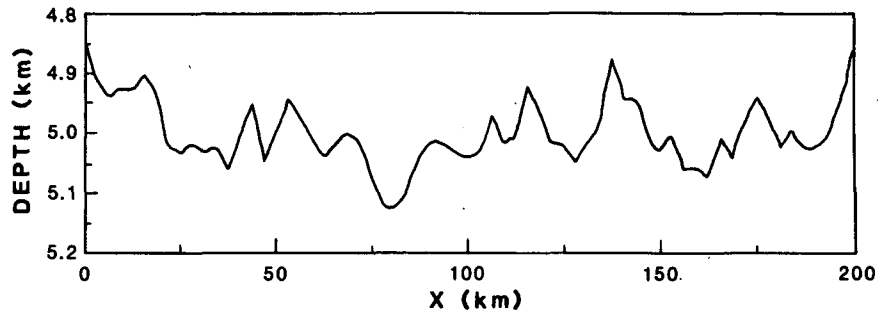

FIG. 10. Realistic bathymetry profile used for case 2 numeric model runs, simulated using the bathymetry model spectrum (3.17).

$$d_j^2 = \int_{(j-1/2)k_x}^{(j+1/2)k_x} S(l)dl, \qquad (5.9)$$

the bathymetry spectrum $S(l)$ is given by (3.17), and the phase terms φ_j are chosen randomly. Thus (5.8) represents a randomly chosen realization of the bathymetry, shown in Fig. 10.

Figure 11 is the w field at time $t = 4t_i$. Comparing with Fig. 7, the fluctuations in w associated with the bathymetry are of similar magnitude. Of course the fluctuations in Fig. 6 are periodic, while those in Fig. 11 are random in the x-direction.

Figure 12 shows a contour map of spectral energy density, as a function of horizontal wavenumber and time, at a depth of 4500 m. The peak energy density at the primary wavenumber 1/200 cpkm dominates the spectrum. There are also two smaller peaks, at the wavenumbers 0.02 and 0.03–0.035 cpkm. These correspond roughly to the sum and difference wavenumbers $l_0 \pm k_x$, where $l_0 = 0.025$ cpkm, $k_x = 0.005$ cpkm. The implication is that energy is scattered primarily into a wavenumber band centered about the roll-off wavenumber l_0. This result is similar to our conclusions in section 3. The upper frames in Figs. 2 and 3 show that the scattering probability density function has a smooth, single peak near l_0. The double peak at $l_0 \pm k_x$ in Fig. 12 results from the discrete, truncated Fourier series (5.8).

6. Summary and discussion

We analyzed the scattering of a large-scale internal wave by an isolated, exceedingly small-scale bump on the ocean floor. Despite an apparent mismatch of scales, kinetic energy density is modulated by the interaction. The energy modulation factor ranged from 0.6 to 1.6. The reason for this strong modulation lies in the comparability of the slope of the bump and the slope of the wave characteristic. A scattered wave, though, has a slower group velocity. It is slower by the ratio of incident to scattered wavenumbers.

We analyzed bottom scattering in the wavenumber domain. The ocean bottom was represented by an em-

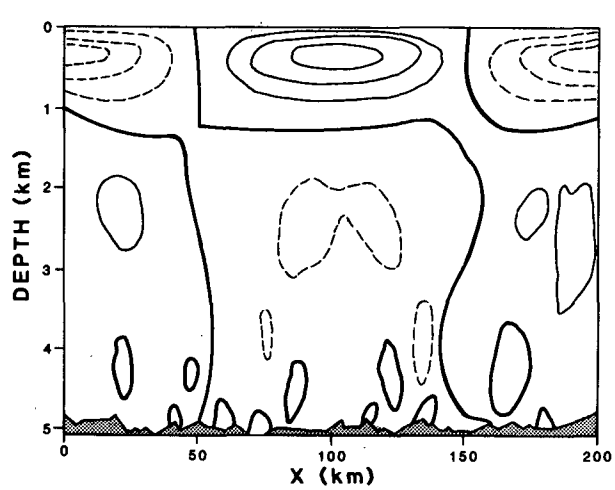

FIG. 11. Vertical velocity field for case 2, at time $4t_i$. Thick curves denote zero, solid/dashed curves denote positive/negative velocities. Contour increment is 0.04 cm s^{-1}. Bathymetry is shown as hatched area.

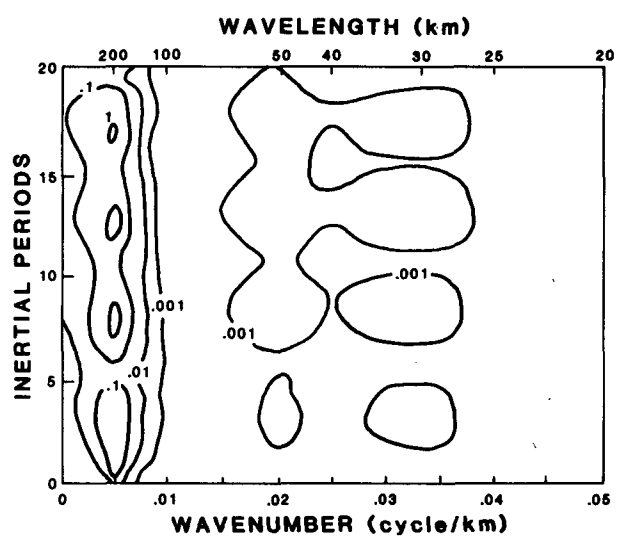

FIG. 12. Contours of kinetic energy spectral density for case 2 at 4500 m depth. Contours have units of m s^{-2} cpkm^{-1} and have logarithmic increments. Contours less than 0.001 are not shown, for clarity.

pirical spectrum. An incident wave with wavelength greater than 150 km is entirely scattered into other, mostly shorter, length scales. None of the incident energy is specularly reflected. Most of the energy flux is scattered into wavelengths comparable to and smaller than the bottom spectrum roll-off wavelength, 40 km.

A Garrett–Munk spectrum of energy flux was applied to the spectral model of rough bottom scattering. Strong bottom interactions cause low-frequency, low-wavenumber waves to be scattered into higher wavenumbers. Incident waves with low wavenumber and high frequency are only weakly scattered. As a result, the vertical wavenumber energy spectrum and the inverse Richardson function corresponding to the scattered wave field were smaller than those of the incident wave field at low wavenumbers, and greater at high wavenumbers. The frequency spectrum is not significantly altered by scattering.

The response to surface forcing was studied using a time dependent numerical model. In the first case treated, a sinusoidal bottom profile, with amplitude 100 m and wavelength 50 km was used. This amplitude is a reasonable value, compared to mesoscale rms elevations. The first vertical mode separates most rapidly from the initial velocity profile. The structure of scattered waves contains higher vertical modes. After 40 inertial periods have elapsed, roughly ⅓ to ½ of the initial energy scatters out of the wavelength of the initial velocity field (200 km) into shorter wavelengths ($\approx$50 km). This fraction corresponds to the fraction (35%) of the energy in the initial velocity profile associated with the first vertical mode.

A second case incorporated a truncated Fourier series, which simulated a realistic bathymetric profile. Energy is scattered primarily into the wavenumber band centered at the bathymetry spectrum roll-off wavenumber, corresponding to 40 km wavelength.

The general conclusion is that after a near-inertial wave field has had sufficient time to reflect from the ocean bottom, most of the energy is scattered into wavelengths comparable to those of the bathymetric features. The 40 km spectral roll-off is important, because it roughly determines the range of scattered wavelengths.

The wavelength of a wind-induced inertial wave is approximately equal to the product of the propagation speed of an atmospheric front and the inertial period (Kundu and Thomson, 1985). Typical observed wavelengths, shortly after the passage of a front, range from 300 to 1500 km (Thomson and Huggett, 1981; Pollard, 1980). More generally though, horizontal coherence scales associated with near-inertial waves are on the order of tens of kilometers, and 50–60 km seems to be an upper limit (Schott, 1971; Fu, 1981). Several mechanisms may contribute to the degradation of coherence from hundreds to tens of kilometers. For example, Rubenstein and Roberts (1986) showed how inertial waves can be scattered by the mesoscale shear structure associated with an ocean front. The scattered waves can have length scales on the order of tens of kilometers, considerably smaller than the horizontal cross-front scale of the shear.

Interactions with bumpy bathymetry can also degrade the coherence scale of inertial waves. Fu (1981) analyzed Polymode observations of inertial waves. He found a tendency for waves observed over smooth topography to be more coherent horizontally, and a tendency for horizontal coherence to decrease with depth. We must be cautious, though, because inertial waves propagate at a shallow angle. They can travel great distances between interactions with the ocean bottom, and locally measured waves may actually have been generated remotely.

The frequency spectrum of internal waves is not significantly altered by rough-bottom scattering. Therefore, records from isolated current meters are not particularly useful for studying the scattering phenomenon. On the other hand, the shape of a vertical wavenumber spectrum of a scattered wave field is significantly less steep than that of an incident field (see Fig. 5). Thus, vertical velocity profilers—with their ability to separate downward and upward propagating wave components—are more useful for studying rough-bottom scattering.

Using velocity profilers, Kunze and Sanford (1986) found a preponderance of upward-propagating near-inertial energy just above and to the sides of the summit of Caryn Seamount. They ruled out bottom generation by a mean flow, because this mechanism would have zero Eulerian frequencies. While not ruling out generation by barotropic tides, they found bottom reflection to be the most likely mechanism. The reason was that the enhancement of upgoing waves over downgoing waves was confined to short vertical wavelengths (<500 m). This result, they point out, is consistent with Eriksen's (1982) ratio of reflected to incident energies

$$\frac{E_r}{E_i} = (k_{z,r}/k_{z,i})^2, \tag{6.1}$$

over a flat, sloping bottom. This result is also consistent with rough-bottom scattering. Figure 5 shows that the spectral level of the scattered wave field is elevated with respect to that of the incident wave field at high wavenumbers.

If we consider 500 m as the vertical wavelength of the reflected wave, then the frequency range 1.01–1.24 f considered by Kunze and Sanford over the seamount summit yields a horizontal wavelength ranging from 42 to 8 km. This range is consistent with the 25 km width of the seamount. This result is evidence of the bumpy bathymetry scattering mechanism, in which reflected energy is modulated over length scales comparable to those of the bottom features. Moreover, the scattering mechanism seems to be relevant here because the seamount is smaller than the wavelength of a typical wind-forced inertial wave. Further evidence of the

scattering mechanism may be found in our theoretical results shown in Fig. 1. Over the isolated bump, upward-propagating energy dominates, in agreement with the measurements by Kunze and Sanford.

Eriksen (1985) points out, with regard to a uniformly sloping bottom, that virtually all of the internal wave field flux may be involved in the reflection process and its subsequent redistribution of energy. This result also applies to the rough-bottom results reported here. Figure 4c shows that a large fraction of the internal wave field is redistributed by rough-bottom interactions. One major difference is that there is no single dominant bottom slope in the present calculations, and therefore no single critical frequency dominates the scattered spectrum. A second difference is that the scattering of waves from high to low wavenumbers is almost negligible, in contrast to Eriksen's calculations showing a reflected flux spectrum that is elevated at low wavenumbers and frequencies higher than the critical frequency. The reason is that the scattered energy flux is proportional to the absolute value of the scattered wavenumber, $k' = |k \pm l/s|$ [see Eq. (3.7)], where l/s is a wavenumber component of the bathymetry, projected onto the incident wave vector which has magnitude k and characteristic slope s. Sum terms are naturally emphasized relative to difference terms.

Eriksen (1985) also shows that reflection from a uniformly sloping bottom is a strong sink for internal wave energy, and may be an important mixing mechanism. This conclusion should be equally true—if not more so—for rough-bottom scattering. Rough-bottom scattering affects the more energetic low-frequency waves more strongly than the less-energetic high-frequency waves, as seen in Fig. 4d. In addition, Fig. 6 shows that the preferred scattering from low to high wavenumbers helps to increase scattered shear—and thus reduce Richardson number and enhance mixing—to a greater degree than would scattering from high to low wavenumbers.

This study has important implications for modeling the evolution of surface-forced inertial waves. Figure 9 shows that the effect of bumpy bathymetry becomes important after 20 inertial periods, and that the first vertical mode is completely scattered into higher modes after 40 inertial periods. Long-term simulations of inertial wave propagation over rough bathymetry should incorporate this effect. The bathymetry might be modeled explicitly in the bottom boundary conditions. Another approach might be to include a dissipation layer, as was done by Rubenstein (1983), to prevent specular reflections off the bottom. A more sophisticated approach would be to parameterize the transfer of energy from the incident wavenumber into higher, bathymetry-related wavenumbers.

Acknowledgments. I thank Lewis Dozier and Eric Kunze for their useful discussions and comments on the manuscript. Support for this work by the Office of Naval Research under Contract N00014-84-C-0221 is gratefully acknowledged.

REFERENCES

Baines, P. G., 1971a: The reflexion of internal/inertial waves from bumpy surfaces. *J. Fluid Mech.*, **46,** 273–291.

——, 1971b: The reflexion of internal/inertial waves from bumpy surfaces. Part 2. Split reflection and diffraction. *J. Fluid Mech.*, **49,** 113–131.

Bell, T. H., 1975a: Statistical features of sea floor topography. *Deep-Sea Res.*, **22,** 883–892.

Eriksen, C. C., 1982: Observations of internal wave reflection off sloping bottoms. *J. Geophys. Res.*, **87,** 525–538.

——, 1985: Implications of ocean bottom reflection for internal wave spectra and mixing. *J. Phys. Oceanogr.*, **15,** 1145–1156.

Fu, L.-L., 1981: Observations and models of inertial waves in the deep ocean. *Rev. Geophys. Space Phys.*, **19,** 141–170.

Gargett, A. E., P. J. Hendricks, T. B. Sanford, T. R. Osborn and A. J. Williams, 1981: A composite spectrum of shear in the upper ocean. *J. Phys. Oceanogr.*, **11,** 1258–1271.

Gill, A. E., 1984: On the behavior of internal waves in the wakes of storms. *J. Phys. Oceanogr.*, **14,** 1129–1151.

Kundu, P. K., and R. E. Thomson, 1985: Inertial oscillations due to a moving front. *J. Phys. Oceanogr.*, **15,** 1076–1084.

Kunze, E., and T. B. Sanford, 1986: Near-inertial wave interactions with mean flow and bottom topography near Caryn Seamount. *J. Phys. Oceanogr.*, **16,** 109–120.

Mied, R. P., and J. P. Dugan, 1976: Internal wave reflexion from a sinusoidally corrugated surface. *J. Fluid Mech.*, **76,** 259–272.

Munk, W. H., 1981: Internal waves and small scale processes. *Evolution of Physical Oceanography,* B. A. Warren and C. Wunsch, Eds., MIT Press, 264–291.

Phillips, O. M., 1963: Energy transfer in rotating fluids by reflection of inertial waves. *Phys. Fluids,* **6,** 513–520.

Pinkel, R., 1985: A wavenumber-frequency spectrum of upper ocean shear. *J. Phys. Oceanogr.*, **15,** 1453–1469.

Pollard, R. T., 1980: Properties of near-surface inertial oscillations. *J. Phys. Oceanogr.*, **10,** 385–398.

Rubenstein, D. M., 1983: Vertical dispersion of inertial waves in the upper ocean. *J. Geophys. Res.*, **88,** 4368–4380.

——, and G. O. Roberts, 1986: Scattering of inertial waves by an ocean front. *J. Phys. Oceanogr.*, **16,** 121–131.

Schott, F., 1971: Spatial structure of inertial-period motions in a two-layered sea, based on observations. *J. Mar. Res.*, **29,** 85–102.

Thomson, R. E., and W. S. Huggett, 1981: Wind-driven inertial oscillations of inertial oscillations of large spatial coherence. *Atmos.-Ocean.*, **19,** 281–306.